

Hematite Surface Activation by Chemical Addition of Tin Oxide Layer

Waldemir M. Carvalho Jr. and Flavio L. Souza*^[a]

In this study, the effect of tin (Sn^{4+}) modification on the surface of hematite electrodes synthesized by an aqueous solution route at different times (2, 5, 10, 18, and 24 h) is investigated. As confirmed from X-ray diffraction results, the as-synthesized electrode exhibits an oxyhydroxide phase, which is converted into a pure hematite phase after being subjected to additional thermal treatment at 750 °C for 30 min. The tin-modified hematite electrode is prepared by depositing a solution of Sn^{4+} precursor on the as-synthesized electrode, followed by thermal treatment under the same abovementioned conditions. This modification results in an enhancement of the photocurrent response for all hematite electrodes investigated and attains the highest values of around 1.62 and 2.3 mA cm^{-2}

at 1.23 and 1.4 V versus RHE, respectively, for electrodes obtained in short synthesis times (2 h). Contact angle measurements suggest that the deposition of Sn^{4+} on the hematite electrode provides a more hydrophilic surface, which favors a chemical reaction at the interface between the electrode and electrolyte. This result generates new perspectives for understanding the deposition of Sn^{4+} on the hematite electrode surface, which is in contrast with several studies previously reported; these studies state that the enhancement in photocurrent density is related to either the induction of an increased donor charge density or shift in the flat-band potential, which favors charge separation.

1. Introduction

For decades, hematite has been attracting attention from the scientific community, as a result of its potential to split water into hydrogen and molecular oxygen under solar irradiation in the photoelectrochemical (PEC) cell configuration.^[1] It is one of the most promising candidates for application as a photoanode in PEC devices, owing to its abundance on earth, low toxicity, good electrochemical stability, and the ability to absorb light in the visible range.^[2] Theoretically, the predicted solar-to-hydrogen efficiency of hematite is 16.8%, and the water-splitting photocurrent is approximately 12.6 mA cm^{-2} .^[3] However, commercial applications of hematite as a photoanode are limited because of its low PEC activity, which is attributed to several factors.^[4] For instance, hematite exhibits a very short minority carrier (hole) diffusion length and poor electronic conductivity, which must be understood for achieving actual progress as a photoanode. With increasing interest in nanoscience, the synthesis of hematite nanostructures has opened up new perspectives for PEC applications of hematite.^[5] Nowadays, the aqueous chemical route under hydrothermal conditions is considered to be a very promising, versatile method for synthesizing films with innumerable morphologies, relatively low cost, and easy scalability.^[4m,5a,6] In addition, the incorporation of tin as a doping element or an overlayer has been intensively re-

ported as a promising alternative for improving the PEC performance of hematite.^[7] For instance, Ling and co-workers reported a significant enhancement of photocurrent for hematite photoanodes synthesized by the aqueous chemical solution method and doped with Sn^{4+} .^[7a] This enhancement in the PEC performance of tin-doped hematite nanostructures is attributed to improvement in electrical conductivity and increased surface area. Later, Xi and co-workers synthesized hematite electrodes by the aqueous chemical route and modified their surfaces by depositing an aqueous solution of Sn^{4+} ; they reported an enhancement of 81% in photocurrent (2.25 mA cm^{-2} at 1.23 V versus RHE), which was attributed to a decrease in the recombination of electrons and holes at the interface between hematite and the electrolyte.^[6h] Recently, Ling and Li published a detailed review and found that a substantial improvement in the PEC performance of hematite was primarily promoted by the incorporation of Sn^{4+} .^[8] However, a complete understanding of the spatial distribution of the Sn^{4+} dopant, shifting of the onset potential, and changes caused in the surface state and in the kinetics of charge transfer at the semiconductor-liquid interface in the hematite nanostructure is still unclear and requires further investigation.^[7b,9]

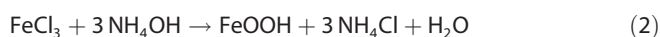
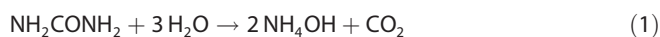
Herein, pure and tin-modified hematite electrodes were synthesized by the aqueous solution route at low temperature under hydrothermal conditions at different times. All electrodes were subjected to additional thermal treatment, which promoted the formation of a desirable hematite phase, as identified by XRD. In addition, the deposition of Sn^{4+} on the hematite electrode surface was investigated by SEM, XRD, and electrochemical measurements to examine surface changes. Contact angle measurements were conducted to obtain a new insight into understanding the effect of tin-modified hematite electrodes.

[a] W. M. Carvalho Jr., Prof. F. L. Souza
Centro de Ciências Naturais e Humanas (CCNH)
Universidade Federal do ABC (UFABC)
09210-580, Santo André, SP (Brazil)
E-mail: fleandro.ufabc@gmail.com
flavio.souza@pq.cnpq.br

Supporting Information for this article can be found under
<http://dx.doi.org/10.1002/cphc.201600316>.

2. Results and Discussion

The growth of aligned 1D nanostructures on fluorine-doped tin oxide (FTO) substrates has been studied because of their unique properties.^[2b,4e,6g,10] The 1D nanostructures exhibit a high surface-to-volume ratio and specific surface crystallographic planes that allow improved catalytic properties. A high photocurrent is commonly attributed to the abovementioned characteristics.^[4e] Vayssieres and co-workers were the first to report the hydrothermal synthesis of hematite 1D nanostructures for PEC applications.^[6a,11] This method attracted attention because it allowed control of morphology without the addition of a surfactant or other salts for increasing ionic strength, templates, and a seed layer. The morphology of the 1D nanostructure was managed by the controlled ionization of urea. Urea exhibits slow ionization, which is controlled by the temperature of the hydrothermal conditions in the reaction system, after reaction with the iron precursor. The ionization of urea and formation of iron oxyhydroxide are summarized in Equations (1) and (2):



The temperature increase during hydrothermal treatment changes the hydrolytic balance, resulting in the formation of ammonium hydroxide [Eq. (1)]. To synthesize iron oxyhydroxide, an increase in temperature changes the enthalpy of hydrolysis in a thermodynamically positive manner, which favors the formation of iron oxyhydroxide [Eq. (2)].^[12] Synthesis under hydrothermal conditions begins with the formation of the first nuclei of oxyhydroxide on the surface of the FTO substrate (Figure 1 a), attributed to favorable heterogeneous nucleation, followed by the total consumption of the reagent; this, in turn, leads to the simultaneous formation of the oxyhydroxide film and powder (see Figure 1 b and Figure S1 in the Supporting Information). Heterogeneous nucleation was more thermodynamically spontaneous, favoring the formation of films and the growth of nanostructures until the energy of the surface of the FTO substrate achieved equilibrium with the environment (Figure 1 b). Moreover, at longer synthesis times (above 10 h), at which the total reagent was consumed and the nanostructures were formed on the conductive glass substrate, a reduction in the diameter of the rods occurred because of redissolution (Figure 1 c). This aqueous solution route under hydrothermal conditions has been discussed in detail in several studies.^[6d,13]

To evaluate the synthetic route, we performed the synthesis at 2, 5, 10, 18, and 24 h, maintaining the solution and substrate under hydrothermal conditions at constant temperature (100 °C). Figure 2 shows SEM images of the films obtained for the as-synthesized, pure, and tin-modified hematite electrodes after 2 h of synthesis under hydrothermal conditions at constant temperature (100 °C) and after additional thermal treatment at 750 °C for 30 min. As shown in Figure 2 a, the image of the as-synthesized electrode (in the oxyhydroxide phase, as identified by XRD data) showed the homogenous distribution of vertical rods on the FTO substrate, with some of the rods

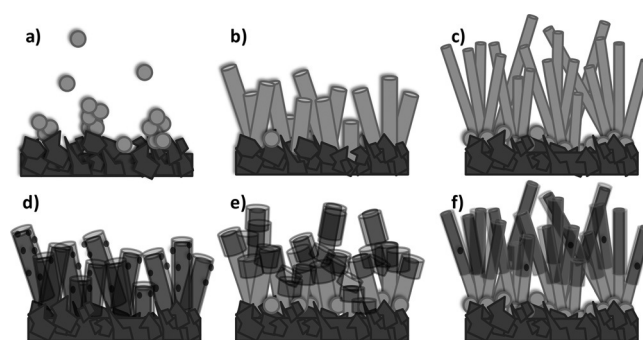


Figure 1. Schematic illustration of the formation of iron oxide rods on a transparent conductive glass substrate: a) the initial step involves the growth of the first iron oxide nuclei on the substrate; b) almost all of the iron source is consumed, resulting in the formation of a mature rod with the maximum diameter and length; and c) a solution of precursor is kept for a long period under hydrothermal conditions, favoring redissolution and decreasing the diameter of the rods. Schematic illustration of iron oxide rods on photoanodes sensitized for d) 2, e) 10, and f) 24 h with a solution of Sn^{4+} and after thermal treatment.

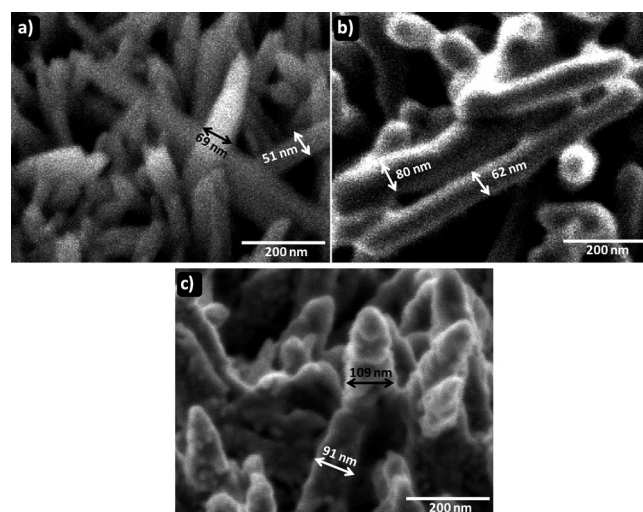


Figure 2. Top-view field-emission (FE) SEM images of a) as-synthesized, b) pure hematite, and c) Sn-modified hematite electrodes synthesized for 2 h. Electrodes in b) and c) were thermally treated at 750 °C for 30 min.

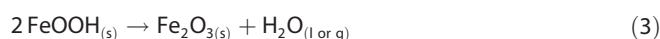
deposited over the layer (parallel to the substrate). For the pure hematite electrode (purity was confirmed by XRD data) obtained after additional thermal treatment, the morphology was unchanged; the image showed the presence of well-distributed rods, with apparent porosity and width increases from 60(3) to 71(2) nm (Figure 2 a and b). In addition, the deposition of an aqueous solution of Sn^{4+} ($70 \mu\text{L}$, 20 mol L^{-1}) on the as-synthesized electrode after being subjected to thermal treatment did not appear to affect the morphology (Figure 2 c). Moreover, from the SEM image shown in Figure 2 c, the hematite electrode surface was homogeneously covered by the deposited solution of Sn^{4+} . The width of the hematite rods increased from 71(2) to 100(8) nm with deposition of the solution of Sn^{4+} after thermal treatment.

For pure hematite electrodes prepared under longer synthetic times (10 and 24 h), the images still showed the presence of rods (see Figure S2a and b in the Supporting Informa-

tion). However, for the as-synthesized films modified with the solution of Sn^{4+} precursor dropped on the yellow layer, the morphology of the electrode abruptly changed after being subjected to thermal treatment at 750°C for 30 min. Modification apparently created a layer over the primary layer, which covered the rods to afford dense plates; these plates looked similar to dried soil (Figure S2 c and d in the Supporting Information). Moreover, the electrodes were evaluated by TEM and high-resolution (HR) TEM (see Figures S6 and S7, respectively, in the Supporting Information). Figures S6a and S7a in the Supporting Information show that the addition of a solution of tin precursor promoted a change in the morphology of the rods. The well-organized and distributed structures of the vertical rods were lost. The presence of small nanoparticles with sizes estimated from HRTEM images to be around 10 nm decorate the hematite nanorods, as illustrated in Figure S7b in the Supporting Information. From HRTEM images, these nanoparticles were indexed as being SnO_2 . Energy-dispersive X-ray (EDX) analysis was performed to obtain chemical information about the energy of the electrodes. EDX analysis confirmed the presence of two different phases: small nanoparticles decorating the rods are composed of the tin oxide phase (cassiterite) and the rods are exclusively hematite phase (Figures S6b and S7c in the Supporting Information). Other interesting information obtained from EDX analysis was that the pure hematite elec-

trode did not exhibit the presence of tin or other chemical contaminants, even when a high thermal treatment temperature was used. This means that there is no diffusion of tin from the substrate to the hematite layer (Figure S6b in the Supporting Information). Indeed, further investigation needs to be conducted to confirm this result.

XRD was employed to examine phase formation, structural parameters, and the effectiveness of the additional thermal treatment for obtaining a pure hematite electrode (Figure 3). Figure 3a shows XRD patterns of the as-synthesized electrode prepared at five synthesis times; the iron oxyhydroxide phase was identified, and the peaks were indexed to characteristic peaks of the iron oxyhydroxide phase of JCPDS card no. 34-1266. In addition, with increasing synthetic times, the peaks observed in Figure 3a became better defined and sharper; this was attributed to an increase in the crystallite size. To obtain the hematite phase, the as-synthesized electrode was subjected to additional thermal treatment at 750°C for 30 min. This temperature was intentionally chosen in accordance with our previously reported study, in which we investigated the effect of temperature on producing high-purity hematite films and powders by the same synthetic route.^[4m,14] The formation of the hematite phase can be expressed by the decomposition of iron oxyhydroxide by thermal treatment according to Equation (3):



Notably, because crystallographic rearrangement occurs from iron oxyhydroxide ($\beta\text{-FeOOH}$) to the hematite phase as a result of thermal treatment, rearrangement does not appear to affect the original morphology (as illustrated by top-view SEM images; Figure 2 and Figure S2 in the Supporting Information). Figure 3b shows the XRD patterns obtained at different synthesis times for pure and tin-modified hematite electrodes after thermal treatment.

The XRD patterns of all pure and tin-modified hematite films shown in Figure 3b were indexed to the characteristic peaks of the hematite phase, corresponding to crystal planes (012) (104) (110) (113), (024), (116), (300), and (233) referenced by using JCPDS card no. 34-0664. Other peaks present in the XRD patterns shown in Figure 3b were assigned to the tin oxide phase (cassiterite phase, SnO_2 ; JCPDS card no. 41-14445) from the conductive layer of the FTO substrate ($\text{SnO}_2\text{:F}$). Indeed, additional peaks corresponding to the solution of Sn^{4+} precursor used for the modification of hematite electrodes were not observed, except for cassiterite observed in the glass conductive substrate layer, which was deposited on the hematite electrode surface. The observation of cassiterite can be attributed to the amount of the tin-deposited source on the hematite layer (below the equipment detection limit), and it can be superposed by the signal of the substrate conductive layer, which is composed of tin oxide (possible phase formed after the films are subjected to additional thermal treatment). Another method for observing the occurrence of doping or any possible modification is to evaluate changes to the unit cell parameters. The unit cell parameters of the hematite structure

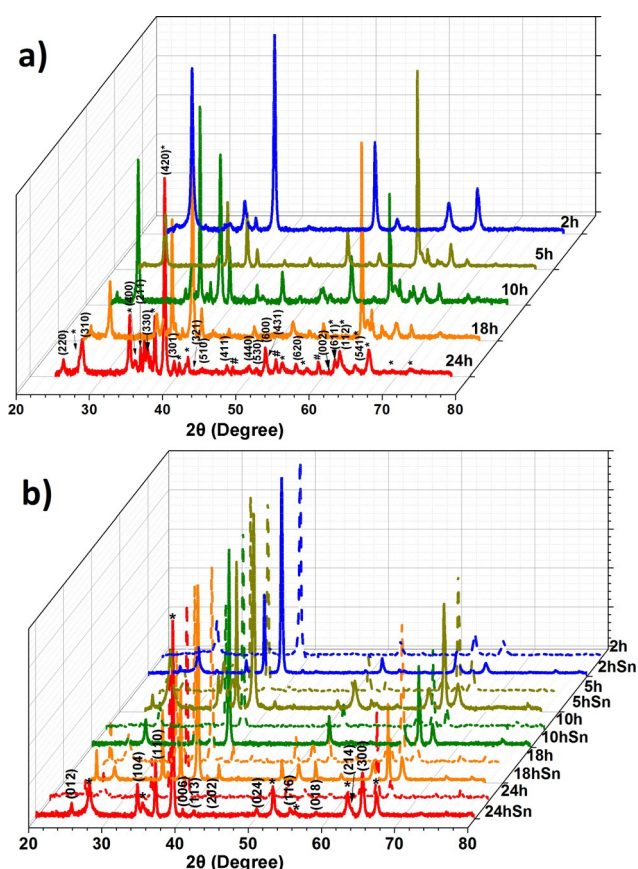


Figure 3. XRD patterns of pure and tin-modified hematite electrodes synthesized for 2, 5, 10, 18, and 24 h under hydrothermal conditions at constant temperature (100°C): a) as-synthesized and b) thermally treated at 750°C for 30 min.

were calculated for all films from the angles and indexed diffraction peaks. All calculations were performed by using free CellCalc software (version 1.51).^[15]

The values obtained for the lattice parameters remained virtually unchanged for the pure and tin-modified hematite electrodes grown at different times with additional thermal treatment. These values were in agreement with those previously reported^[16] for nanostructures of pure hematite electrodes, with *a* and *c* values recorded on JCPDS card no. 33-0664, in-

Samples	<i>a</i> [Å]	Lattice parameter <i>c</i> [Å]	<i>V</i> [Å ³]	O.P.
JCPDS	5.1	13.8	302	
2 h	5.0 ± 0.1	13.2 ± 0.3	279 ± 8	110
2 h(Sn)	5.0 ± 0.1	13.4 ± 0.1	281 ± 3	110
5 h	5.0 ± 0.1	13.4 ± 0.1	282 ± 2	110
5 h(Sn)	5.0 ± 0.1	13.3 ± 0.3	284 ± 5	110
10 h	5.0 ± 0.1	13.3 ± 0.2	284 ± 4	110
10 h(Sn)	5.0 ± 0.1	13.4 ± 0.2	281 ± 3	110
18 h	5.0 ± 0.1	13.4 ± 0.1	285 ± 2	110
18 h(Sn)	5.0 ± 0.1	13.4 ± 0.1	286 ± 2	110
24 h	5.0 ± 0.1	13.5 ± 0.1	290 ± 3	110
24 h(Sn)	5.0 ± 0.1	13.5 ± 0.2	289 ± 4	110

cluding the slight difference in the cell volume (see Table 1). For nanostructures synthesized by the wet route, the estimated values of cell volume were typically less than those observed for standard hematite, which are related to bulk hematite.^[16] However, for tin-modified hematite electrodes, a small reduction in the cell volume was observed (Table 1) relative to that for pure hematite electrodes, as well as that observed in the JCPDS pattern; this was attributed to changes caused by the segregation of the Sn⁴⁺ precursor. The incorporation of different elements during the preparation of hematite films by different chemical methods is known to result in a reduction of crystallite size instead of a desirable doping effect. For instance, the reduction of crystallite size during thermal treatment, which consequently decreases the cell volume, can be attributed to the segregation of incorporated elements preventing crystal growth. This effect has been extensively reported previously.^[5b,17] Moreover, the degree of orientation (*F*) was estimated from the XRD data (Figure 3) by using the equation proposed by Lotgering [Eq. (4)].^[18]

$$F = (P - P_0) / (1 - P_0) \quad (4)$$

in which $P = \sum I(h00) / I(hkl)$, *I* represents the peak intensity from the diffraction pattern obtained experimentally, and *P*₀ represents the *P* value calculated by using data from the JCPDS card of a polycrystalline sample. According to the calculated *P*₀ values summarized in Table 1, all pure and tin-modified hematite electrodes obtained herein exhibited the preferred orientation of crystal growth in the (110) diffraction plane. Notably, the deposition of the solution of tin precursor on the as-synthesized electrodes and additional thermal treatment did not

affect crystal orientation, as observed by the results given in Table 1. Highly oriented hematite nanorods were observed along the [110] direction (parallel to the substrate); this indicates that the basal plane (001) is orthogonal to the substrate, which, in turn, favors charge collection. The orientation of hematite crystals in the [110] direction is known to favor high anisotropic conductivity, estimated at four orders of magnitude, relative to the orientation orthogonal to the growth substrate.^[5g,7a] Indeed, in 2006, Kay and co-workers reported an interesting discussion,^[5g] in which parallel spins were observed for Fe³⁺ atoms within each bilayer, whereas opposite rotation **SPT** as observed for adjacent bilayers. This arrangement allows for the movement of electrons through jumps between Fe atoms within the bilayers, which occurs because of a change of the valence of the Fe atoms between Fe²⁺ and Fe³⁺; this change of valence permits the exchange of electrons between neighboring bilayers, which is spin-forbidden (Hund's rule). This preferred orientation facilitates the transfer of electrons, which increases the collection of photoexcited electrons along the growth axis of nanorods. Among several factors that limit the high electrode performance of hematite, such as considerable hole–electron recombination,^[17,19] the production of nanostructures with well-controlled crystal orientation is efficient for increasing charge transport (hole diffusion and electron collection).^[17,20]

For the application of hematite electrodes in PEC, visible-light absorption is also an important requirement. The as-synthesized and hematite electrodes were evaluated by UV/Vis spectroscopy (Figure S2 in the Supporting Information).

With increasing synthesis time, the as-synthesized electrodes exhibited a decrease in the transmittance rate (%; Figure S2a in the Supporting Information). This reduction, which is strictly dependent on the synthesis time, is attributed to the amount of iron oxide deposited on the conductive glass substrate. For hematite electrodes synthesized for 24 h, the transmittance rate consistently decreased, reaching up to 80%. Moreover, for the pure and tin-modified hematite electrodes, after additional thermal treatment the transmittance decreased further. As expected, the deposition of solutions of Sn⁴⁺ precursor on the hematite electrode surface apparently did not affect the color (red), and only a slight enhancement in the transmittance rate was observed (Figure S2b in the Supporting Information). However, a previous study reported that the addition of Sn⁴⁺ as a dopant enhanced the optical absorption coefficient two-fold; this was attributed to structural distortion in the hematite lattice.^[7a,b]

To evaluate the efficiency of water oxidation for pure and tin-modified hematite electrodes, linear sweep voltammetry (LSV) was conducted in the absence and presence of light by using an electrochemical cell with a three-electrode configuration and a quartz window. Figure 4a and b shows plots of photocurrent density versus applied potential (against RHE) of the pure and tin-modified hematite electrodes under dark and light conditions. During dark conditions (Figure 4a and b, black line), no significant increase in current was observed, except at an applied potential of greater than 1.7 V versus RHE; this was attributed to the electrolysis of water for all

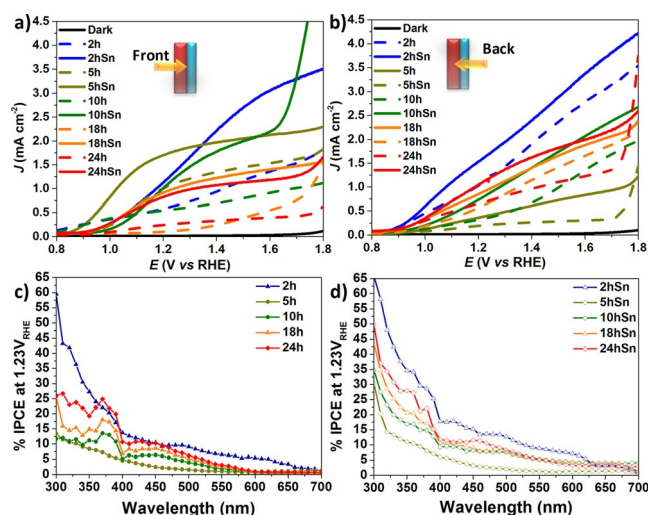


Figure 4. Current density (J , mA cm^{-2}) at an applied potential of 1.23 V versus RHE under a) front and b) back sunlight irradiation at a scan rate of 50 mV s^{-1} for pure and Sn-modified hematite electrodes, and c) and d) Incident-photon-to-current efficiency (IPCE) performed at 1.23 V versus RHE for all hematite electrodes measured in b). Electrolyte: 1 mol L^{-1} of NaOH at pH 13.6.

hematite electrodes. On the other hand, for hematite electrodes under light conditions, a photocurrent response was observed at 0.81 V versus RHE and reached a maximum value at 1.4 V versus RHE. For pure hematite electrodes, the highest photocurrent response was obtained after a synthesis time of 2 h, with values of around 1.12 and 1.54 mA cm^{-2} at 1.23 and 1.4 V versus RHE, respectively (Figure 4a and b, dashed blue line). These values are around 3.0 and 1.6 times higher than those observed under the same conditions for hematite electrodes synthesized for 10 and 24 h, as indicated by olive and red lines, respectively, in Figure 4a and b.

As shown by the solid lines in Figure 4a and b, deposition of the solution of Sn^{4+} precursor on the hematite electrode surface increases the photocurrent response for all pure electrodes synthesized herein. As expected, modification of the electrodes was more effective for those obtained after 2 h, with the photocurrent response reaching 1.62 and 2.30 mA cm^{-2} at 1.23 and 1.4 V versus RHE, respectively (see solid blue lines in Figure 4a and b). In addition, pure and tin-modified hematite electrodes were analyzed by IPCE at 1.23 V versus RHE. IPCE values for pure hematite electrode (2, 10, and 24 h) were estimated at around 42, 13, and 21% at $\lambda = 310 \text{ nm}$ and decreased to 25, 10, and 16% at $\lambda = 400 \text{ nm}$ (solid dots, see Figure 4c and d). Higher IPCE values were obtained for similar tin-modified hematite electrodes, with values reaching 51, 33, and 40% at $\lambda = 310 \text{ nm}$ and 30, 21, and 23% at $\lambda = 400 \text{ nm}$, respectively, as indicated in Figure 4d. Moreover, IPCE data measured at 1.23 V versus RHE were integrated with a standard AM 1.5G (100 mW cm^{-2}) solar spectrum and the calculated photocurrent values of all pure and tin-modified hematite electrodes were very similar to those obtained by the sunlight simulator used. This result can be used to confirm the quality of the calibration of the sunlight simulator used in this study.

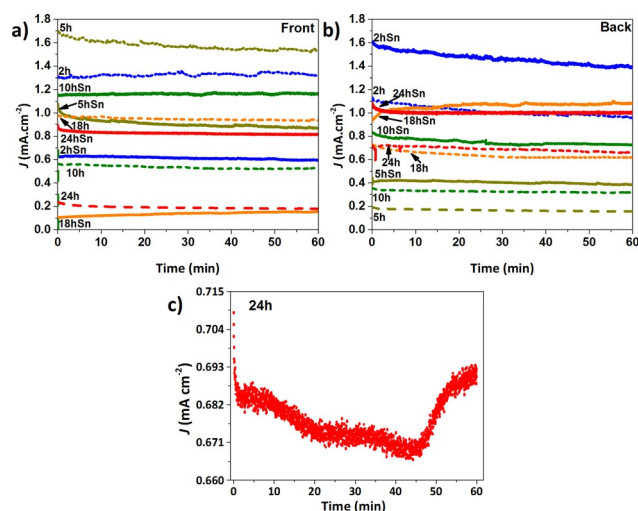


Figure 5. Chronoamperometry (J versus time) under simulated sunlight at 1.23 V versus RHE a) front and b) back illumination for all $\alpha\text{-Fe}_2\text{O}_3$ nanorod films of pure and Sn-modified electrodes, and c) magnification of the curve of the sample synthesized at 24 h.

Long-term stability was investigated at 1.23 V versus RHE for 1 h by chronoamperometry. Excellent stability was observed for all synthesized hematite electrodes with and without modification (Figure 5a and b).

However, different behavior was observed for pure hematite electrode synthesized for 24 h, as represented by a dashed red line in Figure 5c. At the start of the measurement, the curve followed a common profile, with a decrease of less than 10% in the photocurrent response followed by stabilization; however, after 45 min, the photocurrent started to increase (Figure 5c). Measurements conducted to evaluate electrodes with liquid at the interface are known to be strongly dependent on the surface area. In that case, this result suggests changes to the surface area during measurements as a result of increasing electrode wettability. This hypothesis must be primarily investigated because no bubbles were generated or released during the entire measurement to justify this significant change in its profile.

To better understand the chronoamperometry data, contact angle measurements were performed to determine the water affinity or wettability of the electrode surface. The period during which data were acquired was maintained constant at 1 min because angles of the electrodes remained constant at this time. Figure 6 shows the images of the angle formed between the water droplet and hematite electrode surface (pure and modified) acquired at the end of 1 min.

Figure 6 shows the final water contact angles (θ_{final}) determined for pure hematite electrodes; the values were 46.4 , 129.8 , and 51.6° for electrodes synthesized for 2, 10, and 24 h (Figure 6a–e). For the tin-modified hematite electrodes, the contact angle decreased; significant changes were observed for the electrode synthesized for 24 h (see Figure 6f and g). The contact angles of tin-modified hematite electrodes synthesized for 2, 10, and 24 h were 18.3 , 98.7 , and 35.8° , respectively. The contact angle values below 120° indicate that the electrode surface becomes hydrophilic, for example, they exhibit

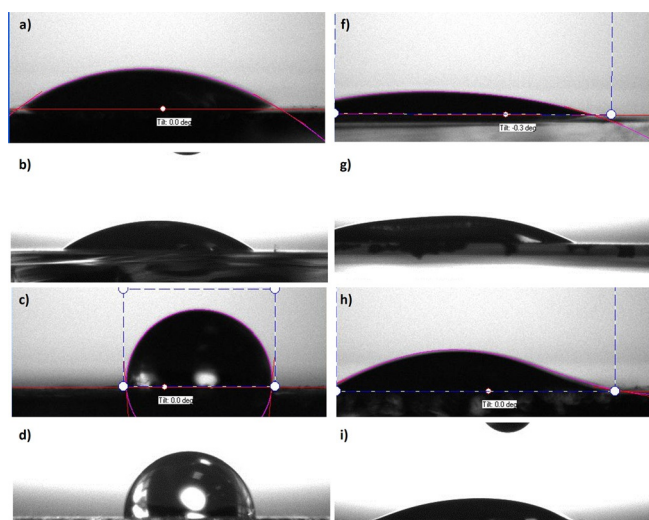


Figure 6. Contact angle images for α - Fe_2O_3 pure nanorod films synthesized for 2 (a), 5 (b), 10 (c), 18 (d), and 24 h (e) and of those from Sn-modified electrodes synthesized for 2 (f), 5 (g), 10 (h), 18 (i), and 24 h (j).

TAB002

more affinity for water (in this case). Table 2 provides a summary of the contact angle values, which show good consistency with the photocurrent response obtained for pure and tin-hematite electrodes. High photocurrent values were observed for electrodes with surfaces that exhibited lower values of contact angle (θ_{final}). The tin-modified hematite electrode synthesized for a shorter time (2 h) exhibited a contact angle of around 18° , which indicated a superhydrophilic surface; this observation corroborates the highest photocurrent response observed. However, for the hematite electrode synthesized at 10 h, higher contact angle values of 129.8 and 98.7° were observed (Table 2), which implied that the surface changed from hydrophobic to partially hydrophilic. This slight change in the surface increases its water affinity, thereby resulting in the enhancement of the photocurrent response of the tin-modified hematite electrode (10 h). Moreover, the strongest decrease in the contact angle observed by comparison between the pure and tin-modified hematite electrodes synthesized for 24 h is attributed to different behavior exhibited during long-term stability tests (chronoamperometry). This result implies that a pure hematite electrode (24 h) needs more time immersed in solution to guarantee effective surface wettability before the start of PEC measurements.

Sample	$\theta_{\text{initial}} [^\circ]$	$\theta_{\text{final}} [^\circ]$
2 h	53.9 ± 0.1	46.4 ± 0.1
2 h(Sn)	23.5 ± 0.1	18.3 ± 0.1
5 h	62.8 ± 0.4	38.0 ± 0.2
5 h(Sn)	46.7 ± 0.3	34.9 ± 0.3
10 h	130.3 ± 0.1	129.8 ± 0.2
10 h(Sn)	107.1 ± 0.1	98.7 ± 0.1
18 h	98.7 ± 0.2	87.4 ± 0.2
18 h(Sn)	57.8 ± 0.1	32.2 ± 0.2
24 h	77.4 ± 0.3	51.6 ± 0.4
24 h(Sn)	39.8 ± 0.5	35.8 ± 0.1

Indeed, the modification used herein, involving the deposition of the solution of tin precursor on the hematite electrode, was effective for increasing surface wettability; the increase in surface wettability consequently enhances the efficiency for water oxidation under sunlight-simulated conditions. Recently, a systematic investigation was conducted, which showed that the temperature of thermal treatment of hematite photoanodes had a strong influence on increasing the wettability and active surface area.^[21] Tin modification changes the film surface to increase the solid/liquid affinity, and thus, the photocurrent.

The electronic properties of pure and tin-modified hematite electrodes were investigated by electrochemical impedance spectroscopy (EIS) and analyzed by Mott–Schottky plots. The values of the flat-band potential (V_{fb}) and donor charge density (N_{D}) were estimated by a combination of the linear regions of the Mott–Schottky plots (see Figure S5 in the Supporting Information) and Equations (5) and (6):

$$\text{slope} = 2/(e\epsilon\epsilon_0N_{\text{D}}A^2) \quad (5)$$

$$V_0 = V_{\text{fb}} + (kT/e) \quad (6)$$

in which e represents the elementary charge of the electron (1.6×10^{-19} C), ϵ represents the dielectric constant of the semiconductor (80 for hematite^[22]), ϵ_0 represents the permittivity of vacuum (8.85×10^{-12} F m⁻¹), A represents the electrode geometric area, V_0 is the fitting linear coefficient ($y=0$), k represent the Boltzmann constant, and T represents the absolute temperature (298 K).

Generally, caution should be exercised while using Mott–Schottky plots of highly porous electrodes because the development of the space-charge regions in the nanostructure may not be the same as that for planar electrodes.^[23] In particular, herein, a good linear fit ($R^2 > 0.99$) of the Mott–Schottky plots for all pure and tin-modified hematite was observed (Figure S5 in the Supporting Information). According to Equation (6), the slope of the plots was inversely proportional to the donor charge density of the semiconductor film. The positive slopes indicate that pure and tin-modified hematite electrodes are n-type semiconductors. The N_{D} values for all pure and tin-modified hematite electrodes do not change significantly and remain at the same order of magnitude (10^{18} cm⁻³). This confirmed that tin deposited on the surface of the hematite electrode did not serve as a dopant, but strictly changed the surface wettability, as observed from the results of contact angle measurements. The use of tin as an overlayer on the hematite electrode is known not to affect the electronic properties,^[8] although when added as a dopant it can enhance the conductivity up to two orders of magnitudes, according to the doping level.^[24] Moreover, the V_{fb} values of pure and tin-modified hematite electrodes were estimated to be between 0.25–0.33 and 0.24–0.5 V versus RHE, respectively. The V_{fb} values obtained for all hematite electrodes were smaller than those previously reported,^[25] except for the values obtained for the pure and tin-modified hematite electrodes synthesized for 10 h, which were higher. This is an unexpected result once the enhancement in flat-band potential values has been reported,

and suggests that the photocurrent increase caused by the deposition of Sn^{4+} contributes to more efficient charge separation. Indeed, herein, the enhancement observed in the photocurrent response with the deposition of Sn^{4+} on the hematite electrode surface was not related to changes in the electronic properties, but was related to improved wettability of the hematite surface. The incorporation of Sn^{4+} increases the water affinity of the hematite surface, which favors the participation of a larger electrode area during PEC measurements compared with that of pure hematite electrodes. Hence, the recombination sites decrease, which consequently increases the electrode efficiency for water oxidation under illuminated conditions.^[6k]

3. Conclusions

Transparent hematite electrodes were synthesized at low temperature in a single step under hydrothermal conditions. Pure hematite electrodes exhibited well-distributed rods on the conductive substrate. At synthesis times of 2 and 5 h, the Sn-modified hematite electrode retained the presence of rods, but involved Sn^{4+} modification. In contrast, for synthesis times of 10 and 24 h, a different morphology of blocks was observed for the Sn-modified hematite electrode; this was attributed to the deposition of the solution of Sn^{4+} precursor, which looked similar to dried soil with several cracks. The addition of Sn^{4+} enhanced the photocurrent response of all hematite electrodes relative to that of pure electrodes; the highest values of 1.12 and 2.3 mA cm^{-2} at 1.23 and 1.4 V versus RHE, respectively, were attained for electrodes synthesized at shorter synthesis times. The improvement in the photocurrent by the addition of Sn^{4+} could provide a more hydrophilic hematite surface (high water affinity), favoring the chemical reaction at the solid–liquid interface and probably reducing the recombination sites. However, a better result could be achieved if actuate was used as a dopant instead of forming an additional phase, as identified by TEM/EDX analysis. These results pave the way for new perspectives to explain the effect of the addition of Sn^{4+} as an overlayer on hematite electrodes. Currently, experiments to further improve the photocurrent response of hematite electrodes are underway in our laboratory.

Experimental Section

Sample Preparation

Pure iron oxide films and those modified by a solution of tin were grown on FTO substrates by a typical procedure in an aqueous solution under hydrothermal conditions.^[4m] This method consisted of preparing an aqueous solution (100 mL) of $\text{FeCl}_3 \cdot 6\text{H}_2\text{O}$ ($1.5 \times 10^{-3} \text{ mol L}^{-1}$; Mallinckrodt) and urea ($1.5 \times 10^{-3} \text{ mol L}^{-1}$; Nuclear). The solution was homogenized until a translucent yellow color was obtained, and then the solution was transferred to a 100 mL Schott bottle. Conductive substrates were placed on a Teflon holder and immersed in the solution contained in the flask and closed. This system was subjected to hydrothermal treatment for 2, 5, 10, 18, and 24 h in a conventional oven at 100°C (Figure S1 in the Supporting Information). The yellow films obtained were

cleaned several times with water to remove excess residues of the precursor salts. After synthesis, the films were heat-treated at 750°C for 30 min with heating and cooling rates of 4°C min^{-1} to give pure $\alpha\text{-Fe}_2\text{O}_3$ films. For tin-modified iron oxide films before thermal treatment, a freshly prepared 20 mmol L^{-1} aqueous solution ($70 \mu\text{L}$) of $\text{SnCl}_4 \cdot 5\text{H}_2\text{O}$ (Vetec) was applied on the yellow layer. After deposition of the solution of Sn^{4+} , the films were maintained in a horizontal position for 5 min at room temperature and subsequently thermally treated at 750°C .

Structural and Morphological Characterization

Crystalline phases of the films thus prepared were characterized by XRD with $\text{Cu K}\alpha$ radiation (DRX-D8 Focus, Bruker AXS) at 2θ ranging from 10 to 80° , with a step scan of 0.02° and 5 s per step. The morphology of the films was examined by SEM (SEM-JSM-6010LA, JEOL). Optical characterization was performed on a Varian Cary 50 spectrophotometer (from $\lambda = 200$ to 1000 nm). The transmittance of the films was measured against air as the reference. For HRTEM coupled to EDX analysis, a Tecnai F20 FEI instrument was used, operating at 200 kV. The sample removed from the substrate were dispersed in ethanol and dropped onto a carbon-coated copper commercial grid. Analysis was conducted after the samples were dried under a UV lamp.

PEC Measurements and Electrochemical Analysis

Electrochemical measurements were conducted by using a three-electrode cell with a quartz window coupled to a potentiostat/galvanostat ($\mu\text{Autolab III}$). For this analysis, iron oxide films, Ag/AgCl in saturated KCl, and platinum foil were used as the working, reference, and counter electrodes, respectively. An aqueous solution of 1 mol L^{-1} NaOH (pH 13.6, Sigma–Aldrich, 99.9%) was used as the electrolyte. LSV (current density versus applied potential) was performed under dark and sunlight-simulated conditions at a scan rate of 50 m s^{-1} . Chronoamperometry (current versus time) was conducted at 1.23 V versus RHE under sunlight-simulated conditions. Sunlight conditions were simulated by using a 450 W xenon lamp (Osram, ozone-free) and an AM 1.5 filter, and the light intensity was set to 100 mW cm^{-2} . The measured potentials versus Ag/AgCl were converted to the RHE scale according to the Nernst Equation [Eq. (7)]:

$$E_{\text{RHE}} = E_{\text{Ag/AgCl}} + 0.059\text{pH} + E^\circ_{\text{Ag/AgCl}} \quad (7)$$

in which E_{RHE} represents the converted potential versus RHE, $E^\circ_{\text{Ag/AgCl}} = 0.1962 \text{ V}$ at 25°C , and $E_{\text{Ag/AgCl}}$ represents the experimentally measured potential against the Ag/AgCl reference electrode. EIS measurements were conducted by using a potentiostat/galvanostat (Autolab PGSTAT129N) coupled to a Faraday cage and analyzed by Mott–Schottky plots (C^{-2} versus V). The Mott–Schottky analysis was performed at a direct current (DC) potential range of 0.2 – 1.8 V versus RHE with an alternating current (AC) potential frequency of 10 kHz under dark conditions; the amplitude of the AC potential was 10 mV . The IPCE was measured as a function of the excitation wavelength (λ) by using a 300 W ozone-free xenon lamp coupled to a Cornerstone 260 monochromator (Oriel quantum efficiency measurement kit). IPCE was calculated by using Equation (8):

$$\text{IPCE} = [I(\lambda)1240/E(\lambda)\lambda] \times 100 \quad (8)$$

in which $I(\lambda)$ represents the photocurrent density (μAcm^{-2}) and $E(\lambda)$ represents irradiance (μWcm^{-2}).

Contact Angle Analysis

The water contact angles of the films were measured after drying the samples for 24 h at 80 °C in a conventional oven followed by cooling in a desiccator. Static contact angles were measured by using a sessile drop at three points of each film with a commercial drop-shape analysis system (Attension Optical Tensiometer, Theta Lite, KSV CAM101) at ambient temperature (25 °C). The contact angle was monitored and calculated for a period of 1 min, and the values were an average between the left and right values.

Acknowledgements

We gratefully acknowledge financial support from the Brazilian agencies of FAPESP (grants 2011/19924-2, 2013/05471-1, and 2014/50516-6), CAPES, CNPq (grant no. 304571/2012-1), CEM-UFABC and CDMF (grant no. 2013/07296-2).

Keywords: doping · electrochemistry · iron · surface analysis · tin

- [1] J. Su, L. Vayssieres, *ACS Energy Letters* **2016**, 121–135.
- [2] a) S. Shen, M. Li, L. Guo, J. Jiang, S. S. Mao, *J. Colloid Interface Sci.* **2014**, 427, 20–24; b) X. Zhou, J. Lan, G. Liu, K. Deng, Y. Yang, G. Nie, J. Yu, L. Zhi, *Angew. Chem. Int. Ed.* **2012**, 51, 178–182; *Angew. Chem.* **2012**, 124, 182–186.
- [3] A. B. Murphy, P. R. F. Barnes, L. K. Randeniya, I. C. Plumb, I. E. Grey, M. D. Horne, J. A. Glasscock, *Int. J. Hydrogen Energy* **2006**, 31, 1999–2017.
- [4] a) M. G. Walter, E. L. Warren, J. R. McKone, S. W. Boettcher, Q. Mi, E. A. Santori, N. S. Lewis, *Chem. Rev.* **2010**, 110, 6446–6473; b) T. R. Cook, D. K. Dogutan, S. Y. Reece, Y. Surendranath, T. S. Teets, D. G. Nocera, *Chem. Rev.* **2010**, 110, 6474–6502; c) M. J. Katz, S. C. Riha, N. C. Jeong, A. B. F. Martinson, O. K. Farha, J. T. Hupp, *Coord. Chem. Rev.* **2012**, 256, 2521–2529; d) K. Maeda, *J. Photochem. Photobiol. C* **2011**, 12, 237–268; e) C. X. Kronawitter, L. Vayssieres, S. Shen, L. Guo, D. A. Wheeler, J. Z. Zhang, B. R. Antoun, S. S. Mao, *Energy Environ. Sci.* **2011**, 4, 3889; f) Á. Valdés, J. Brillet, M. Grätzel, H. Gudmundsdóttir, H. A. Hansen, H. Jónsson, P. Klüpfel, G.-J. Kroes, F. Le Formal, I. C. Man, R. S. Martins, J. K. Nørskov, J. Rossmeisl, K. Sivula, A. Vojvodic, M. Zäch, *Phys. Chem. Chem. Phys.* **2012**, 14, 49–70; g) R. van de Krol, Y. Liang, J. Schoonman, *J. Mater. Chem.* **2008**, 18, 2311; h) B. D. Alexander, P. J. Kulesza, I. Rutkowska, R. Solarzka, J. Augustynski, *J. Mater. Chem.* **2008**, 18, 2298–2303; i) K. Sivula, F. Le Formal, M. Grätzel, *ChemSusChem* **2011**, 4, 432–449; j) Y. Tachibana, L. Vayssieres, J. R. Durrant, *Nat. Photonics* **2012**, 6, 511–518; k) K. Shankar, J. I. Basham, N. K. Allam, O. K. Varghese, G. K. Mor, X. Feng, M. Paulose, J. A. Seabold, K.-S. Choi, C. A. Grimes, *J. Phys. Chem. C* **2009**, 113, 6327–6359; l) R. M. Navarro, M. C. Alvarez-Galvan, J. A. Villoria de La Mano, S. M. Al-Zahrani, J. L. G. Fierro, *Energy Environ. Sci.* **2010**, 3, 1865–1882; m) W. M. Carvalho, Jr., F. L. Souza, *J. Mater. Res.* **2014**, 29, 16–28.
- [5] a) L. Vayssieres, N. Beermann, S.-E. Lindquist, A. Hagfeldt, *Chem. Mater.* **2001**, 13, 233–235; b) F. L. Souza, K. P. Lopes, P. A. P. Nascente, E. R. Leite, *Solar Energy Materials and Solar Cells* **2009**, 93, 362–368; c) R. H. Gonçalves, B. H. R. Lima, E. R. Leite, *J. Am. Chem. Soc.* **2011**, 133, 6012–6019; d) T. Hisatomi, H. Dotan, M. Stefiik, K. Sivula, A. Rothschild, M. Grätzel, N. Mathews, *Adv. Mater.* **2012**, 24, 2699–2702; e) T. Hisatomi, J. Brillet, M. Cornuz, F. Le Formal, N. Tetreault, K. Sivula, M. Grätzel, *Faraday Discuss.* **2012**, 155, 223–232; f) I. Cesar, A. Kay, J. A. G. Martinez, M. Grätzel, *J. Am. Chem. Soc.* **2006**, 128, 4582–4583; g) A. Kay, I. Cesar, M. Grätzel, *J. Am. Chem. Soc.* **2006**, 128, 15714–15721; h) J. Brillet, M. Grätzel, K. Sivula, *Nano Lett.* **2010**, 10, 4155–4160; i) K. Sivula, R. Zboril, F. Le Formal, R. Robert, A. Weidenkaff, J. Tucek, J. Frydrych, M. Grätzel, *J. Am. Chem. Soc.* **2010**, 132, 7436–7444; j) J. Deng, X. Lv, J. Gao, A. Pu, M. Li, X. Sun, J. Zhong, *Energy Environ. Sci.* **2013**, 6, 1965–1970; k) D. Wodka, R. P. Socha, E. Bielańska, M. Elźbięciak-Wodka, P. Nowak, P. Warszyński, *Applied Surface Science* **2014**, 319, 173–180.
- [6] a) N. Beermann, L. Vayssieres, S.-E. Lindquist, A. Hagfeldt, *J. Electrochem. Soc.* **2000**, 147, 2456–2461; b) L. Vayssieres, C. Sathe, S. M. Butorin, D. K. Shuh, J. Nordgren, J. Guo, *Adv. Mater.* **2005**, 17, 2320–2323; c) R. Morrish, M. Rahman, J. M. Don MacElroy, C. A. Wolden, *ChemSusChem* **2011**, 4, 474–479; d) D. K. Bora, A. Braun, R. Erni, G. Fortunato, T. Graule, E. C. Constable, *Chem. Mater.* **2011**, 23, 2051–2061; e) V. A. N. de Carvalho, R. A. S. Luz, B. H. Lima, F. N. Crespilho, E. R. Leite, F. L. Souza, *J. Power Sources* **2012**, 205, 525–529; f) M. Cornuz, M. Grätzel, S. Kevin, *Chem. Vap. Deposition* **2010**, 16, 291–295; g) L. C. Ferraz, W. M. Carvalho, Jr., D. Criado, F. L. Souza, *ACS Appl. Mater. Interfaces* **2012**, 4, 5515–5523; h) L. Xi, S. Y. Chiam, W. F. Mak, P. D. Tran, J. Barber, S. C. J. Loo, L. H. Wong, *Chem. Sci.* **2013**, 4, 164–169; i) X. Zong, S. Thaweesak, H. Xu, Z. Xing, J. Zou, G. Lu, L. Wang, *Phys. Chem. Chem. Phys.* **2013**, 15, 12314–12321; j) C. Zheng, Z. Zhu, S. Wang, Y. Hou, *Applied Surface Science* **2015**, 359, 805–811; k) D. Xu, Y. Rui, Y. Li, Q. Zhang, H. Wang, *Appl. Surf. Sci.* **2015**, 358, 436–442.
- [7] a) Y. Ling, G. Wang, D. A. Wheeler, J. Z. Zhang, Y. Li, *Nano Lett.* **2011**, 11, 2119–2125; b) Z. Cao, M. Qin, Y. Gu, B. Jia, P. Chen, X. Qu, *Mater. Res. Bull.* **2016**, 77, 41–47; c) P. S. Shinde, A. Annamalai, J. H. Kim, S. H. Choi, J. S. Lee, J. M. S. Jang, *Sol. Energy Mater. Sol. Cells* **2015**, 141, 71–79.
- [8] Y. Ling, Y. Li, *Part. Part. Syst. Charact.* **2014**, 31, 1113–1121.
- [9] a) Y. Ling, G. Wang, J. Reddy, C. Wang, J. Z. Zhang, Y. Li, *Angew. Chem. Int. Ed.* **2012**, 51, 4074–4079; *Angew. Chem.* **2012**, 124, 4150–4155; b) M. Barroso, S. R. Pendlebury, A. J. Cowan, J. R. Durrant, *Chem. Sci.* **2013**, 4, 2724–2734.
- [10] S. Li, G. W. Qin, Y. Zhang, W. Pei, L. Zuo, C. Esling, *Anv. Enign. Mater.* **2010**, 12, 1082–1085.
- [11] L. Vayssieres, A. Hagfeldt, S. E. Lindquist, *Pure Appl. Chem.* **2000**, 72, 47–52.
- [12] R. G. Robins, *J. Inorg. Nucl. Chem.* **1967**, 29, 431–435.
- [13] a) F. L. Souza, A. M. Xavier, W. M. Carvalho, R. H. Gonçalves, E. R. Leite in *Nanoenergy: Nanotechnology for Energy Production* (Eds.: F. L. Souza, E. R. Leite), Springer, Berlin, **2013**, pp. 81–99; b) K. Byrappa, M. Yoshimura, *Handbook of Hydrothermal Technology*, William Andrew Publishing, Norwich, **2001**, pp. 1–52.
- [14] A. M. Xavier, F. F. Ferreira, F. L. Souza, *RSC Adv.* **2014**, 4, 17753–17759.
- [15] H. MIURA, Ver. 1.51, Department of Earth and Planetary Sciences, Graduate School of Science Hokkaido University; a Windows program to calculate unit cell parameters and their standard deviations from observed d values and hkl data.
- [16] M. Gaudon, N. Pailhé, J. Majimel, A. Wattiaux, J. Abel, A. Demourgues, *J. Solid State Chem.* **2010**, 183, 2101–2109.
- [17] F. L. Souza, K. P. Lopes, E. Longo, E. R. Leite, *Phys. Chem. Chem. Phys.* **2009**, 11, 1215–1219.
- [18] a) D. M. Cunha, F. L. Souza, *J. Alloys Compd.* **2013**, 577, 158–164; b) T. Ami, M. Suzuki, *Mater. Sci. Eng. B* **1998**, 54, 84–91.
- [19] P. S. Shinde, S. H. Choi, Y. Kim, J. Ryu, J. S. Jang, *Phys. Chem. Chem. Phys.* **2016**, 18, 2495–2509.
- [20] S. Shen, C. X. Kronawitter, J. Jiang, S. S. Mao, L. Guo, *Nano Res.* **2012**, 5, 327–336.
- [21] W. M. Carvalho, Jr., F. L. Souza, *Solar Energy Materials and Solar Cells* **2016**, 144, 395–404.
- [22] S. U. M. Khan, J. Akikusa, *J. Phys. Chem. B* **1999**, 103, 7184–7189.
- [23] a) A. d. S. Gonçalves, M. R. Davolos, A. F. Nogueira, *J. Nanosci. Nanotechnol.* **2010**, 10, 6432–6438; b) R. H. Gonçalves, L. D. T. Leite, E. R. Leite, *ChemSusChem* **2012**, 5, 2341–2347.
- [24] A. Annamalai, P. S. Shinde, T. H. Jeon, H. H. Lee, H. G. Kim, W. Choi, J. S. Jang, *Sol. Energy Mater. Sol. Cells* **2016**, 144, 247–255.
- [25] A. L. M. Freitas, W. M. Carvalho, Jr., F. L. Souza, *J. Mater. Res.* **2015**, 30, 3595–3604.

Manuscript received: March 28, 2016

Accepted Article published: May 30, 2016

Final Article published: June 17, 2016